Table S1 to accompany Figure 3. AIF78 Monomer and W196A X-ray Diffraction and Refinement Parameters

	AIF78 E413A/R422A/R430A	**AIF78 W196A**
Space Group	$P2_12_12_1$	$P2_12_12_1$
Unit Cell Parameters (Å)	a = 64.6, b = 81.8, c = 108.3 α = β = γ = 90	a = 89.8, b = 112.2, c = 122.2 α = β = γ = 90
Data Collection		
Temperature (K)	100	100
Wavelength (Å)	0.9762	0.9762
Resolution (Å)	27.7-2.0	60.82-2.27
Total reflections	200938	404472
Unique reflections	31986 (1338)	57030 (5340)
Mean I/σ(I)	18.1 (2.3)	10.0 (0.7)
Completeness (%)	80.1 (31.6)	100.0 (100.0)
Redundancy	6.3 (2.3)	7.0 (7.1)
Rsym (%)	9.0 (38.1)	20.1 (275)
CC1/2	N/A	0.995 (0.395)
Data Refinement		
Resolution range (Å)	45.16 – 2.00	60.7 – 2.27
Number of atoms	4194	7494
Protein	3665	6699
Ligand	74	112
Solvent	479	876
Rwork (%) / Rfree (%)	15.7 / 19.4	20.2 / 24.0
RMS Deviations		
Bond Length (Å)	0.008	0.002
Bond Angles (°)	0.95	0.44
Average B-factor (Å^2)	34.8	45.09
Ramachandran Analysis		
In favored regions (%)	97.0	96.0
In allowed regions (%)	3.4	3.6
Outliers (%)	0	0.2

*Values in parentheses are for the highest resolution shell.

Supplemental Experimental Procedures

Materials

The AIFM1 plasmid was obtained from the DNASU Plasmid Repository (Cormier et al., 2010; Seiler et al., 2014). Methoxypolyethylene glycol (mPEG) – maleimide (MEM) (10 kDa) was purchased from Laysan Bio and prepared according to the manufacturer's directions. Bis(sulfosuccinimidyl) suberate (BS^3) was purchased from Thermo Scientific. Proteinase K solution (20 mg/mL) was purchased from Worthington Biochemical Corporation. Reduced NADH was purchased from Sigma-Aldrich, resuspended at 100 mM in 25 mM HEPES, pH 8, aliquoted and stored at -80°C.

Subcloning, Expression and Purification of Wild-type and Mutant AIF

All AIF constructs were subcloned into the pET24b vector with C-terminal Prescission protease cleavage site and 6X histidine affinity tag. AIF point mutants were generated by Gibson assembly. Wild-type AIF constructs and mutants were grown in Rosetta2 (DE3) cells (Novagen, EMD Millipore) at 37 °C to OD_{600} 0.5-0.6 and expressed for 3 hours after IPTG induction. All constructs were purified by nickel affinity chromatography (GE HisTrap HP 5 mL or GOLDBIO.COM High Density Nickel resin) in buffer containing 25 mM HEPES (pH 8.0), 250 mM NaCl, and 10 mM imidazole with a linear elution gradient of 30-300 mM imidazole (GE HisTrap) or block elution in 300 mM imidiazole (GOLDBIO.COM Nickel resin). Fractions containing protein were pooled with 6X-histidine-tagged Prescission protease, dialyzed in 25 mM HEPES (pH 8.0), 200 mM NaCl, and 5 mM β-mercaptoethanol (βME) overnight at 4°C, and repassed over nickel affinity resin to remove the cleaved histidine fusion tag and protease. Constructs were concentrated and purified by size-exclusion chromatography on a HiLoad Superdex 200 26/60 or HR Superdex 200 10/30 column in 25 mM HEPES (pH 8.0), 200 mM NaCl, and 5% glycerol. Protein fractions were scanned and selected for A_{270}/A_{450} 7-8 and $A_{260}/_{280}$ ~0.8 to ensure proper incorporation of the FAD cofactor. The concentration of AIF dimer-permissive mutants was also verified by Bradford assay. Fractions were pooled and concentrated, then aliquoted and flash frozen in liquid nitrogen for storage at -80°C.

NADH Oxidation Assays

Reactions (500 µL) of 10 uM AIF and 50 uM NADH in 25 mM HEPES, pH 7.5, 150 mM NaCl were scanned from 200-800 nm at 0, 2.5, 5, 10, 15, 20 minutes following mixing at room temperature with a Cary 50 Bio UV-visible spectrophotometer.

Limited Proteolysis Experiments

Reactions (20 µL) of 10 µM AIF and 0-20-fold molar excess NADH were prepared in 25 mM HEPES, pH 7.5, 150 mM NaCl and incubated for 10-15 minutes at room temperature to allow charge-transfer complex formation. Proteinase K was added to 5 µg/mL and allowed to digest for 30 minutes at room temperature. Reactions were quenched by combining 3 uL of the reaction mixture with 10 uL 3X SDS loading buffer, boiling for 1-2 minutes, and running the reaction out on a 10% SDS-PAGE gel.

Cross-Linking Experiments

Reactions (20 µL) of 10 µM AIF and 0-20-fold molar excess NADH were prepared in 25 mM HEPES, pH 7.5, 150 mM NaCl and incubated for 10-15 minutes at room temperature to allow charge-transfer complex formation. BS^3 (bis(sulfosuccinimidyl)suberate) cross-linker was added to 1 mM and allowed to cross-link for 30 minutes at room temperature. Reactions were quenched by combining 3 uL of the reaction mixture with 10 uL 3X SDS loading buffer, boiling for 1-2 minutes, and running the reaction out on a 4-15% gradient SDS-PAGE gel.

PEG-MEM Labeling

Reactions (20 µL) of 33 µM AIF78 WT, R422C, R449C and 0-, 1- or 10-fold molar excess NADH were prepared in 25 mM HEPES, pH 7.0, 150 mM NaCl and incubated for 15 minutes at room temperature to allow charge-transfer complex formation. PEG-MEM was added to ~330 µM (10-fold excess) and allowed to react for 30 minutes at room temperature. Reactions were quenched by combining 3 uL of the reaction mixture with 10 uL 3X SDS loading buffer, boiling for 1-2 minutes, and running the reaction out on a 10% SDS-PAGE gel.

Small-angle X-ray Scattering (SAXS) Sample Preparation, Data Collection and Analysis, and AIF Modeling

Purified wild-type or mutant AIF was concentrated to 20-30 mg/mL and loaded onto a HR Superdex 200 10/30 column equilibrated in 25 mM HEPES, pH 7.5, 150 mM NaCl. Fractions at the maxima of the eluted peaks were selected to prepare concentration series and NADH titration samples for SAXS analysis. Concentration series were prepared in buffer collected from the corresponding void volume of the gel filtration run. NADH titration series were prepared by direct addition of 0-10-fold molar excess NADH to either AIF protein (3-4 mg/mL) or buffer blanks to be used for buffer subtraction. Samples were transferred to a 96-well plate, frozen in liquid nitrogen or dry ice, and shipped overnight for data collection.

SAXS data were collected at the ALS beamline 12.3.1 LBNL Berkeley, California (Classen et al., 2013). X-ray wavelength λ 1.03 Å and the sample-to-detector distances were set to 1.5 m resulting in scattering vectors, q, ranging from 0.01 $Å^{-1}$ to 0.33 $Å^{-1}$. The scattering vector is defined as $q = 4\pi \sin\theta/\lambda$, where 2θ is the scattering angle. All experiments were performed at 20°C (Dyer et al., 2014).

SAXS data were assessed for radiation-dependent aggregation and analyzed using the Atsas Primus module (Petoukhov et al., 2012) and Scatter (v. 2.3h). R_g values for concentration series were derived from Guinier analysis and remained stable for wild-type AIF and monomeric AIF mutants. Dimer-permissive AIF mutants exhibited a concentration-dependent rise in R_g consistent with dimer formation. Molecular envelope calculations were performed with DAMMIF (Franke and Svergun, 2009); ten DAMMIF runs were averaged in DAMAVER to produce the final envelope (Volkov and Svergun, 2003). SAXS envelopes for AIF monomer (PDB: 4BV6) and dimer (PDB: 4BUR) crystal structures were calculated in a similar manner using theoretical scattering curves generated by the FoXS server (Schneidman-Duhovny et al., 2013). AIF mass estimates derived from volumes of correlation (V_c) were calculated following the method outlined in (Rambo and Tainer, 2013). SAXS similarity matrices (SSM) were generated using the SAXS similarity webapp hosted by the ALS SIBYLS beamline (http://sibyls.als.lbl.gov/saxs_similarity/) (Hura et al., 2013). SAXS data from this publication are deposited at sibyls.als.lbl.gov/saxs_similarity/ and are being submitted to the BIOSIS database (http://bioisis.net).

AIF models used for analyzing SAXS data were prepared from coordinates of AIF crystal structures (above); missing C-loop or N-terminal residues were added in Chimera (Pettersen et al., 2004). Models were passed through the BilboMD sampling server to identify C-loop or termini conformations of best-fit to the scattering data (Pelikan et al., 2009). Application of a minimal ensemble search (MES) (described in (Pelikan et al., 2009)) showed only moderate improvement in the fit to the data when two or more models were considered. Theoretical scattering curves were calculated with the FoXS server and compared to the experimental scattering data by χ goodness-of-fit. Best-fitting AIF models selected by BilboMD were manually placed into SAXS envelopes with Chimera (Pettersen et al., 2004).

AIF Crystallization, Data Collection, and Structure Determination

AIF78 Monomer (E413A/R422A/R430A) and AIF78 W196A crystals were grown by hanging drop vapor diffusion with equal parts protein solution (Monomer 15 mg/mL, W196A 10mg/mL) and well solution (Monomer: 100 mM HEPES, pH 7.5, 50 mM NaCl, 24% PEG3350; W196A: 300 mM Na_2SO_4, 16% PEG3350) at 18 °C. Crystals were briefly equilibrated in cryo-protectant solution containing 10% glycerol, 100 mM Tris, pH 7.5, 50 mM NaCl, 24% PEG3350 (AIF78 Monomer) or 15% glycerol, 100 mM Tris, pH 7.5, 150 mM NaCl, 20% PEG3350 (AIF78 W196A), then flash-cooled in liquid nitrogen. X-ray diffraction data were collected at beamline 4.2.2 at the Advanced Light Source (ALS) at LBNL. AIF78 Monomer ($P2_12_12_1$, a = 64.3 Å, b = 81.6 Å, c = 108.0 Å, α=β=γ=90°; one AIF molecule per asymmetric unit) diffracted to 2.0 Å resolution, based on $I/\sigma(I) > 2.0$, and AIF78 W196A ($P2_12_12_1$, a = 90.2 Å, b = 112.9 Å, c = 121.3 Å, α=β=γ=90°; two AIF molecules per asymmetric unit) diffracted to 2.27 Å resolution, based on a CC1/2 cutoff of 0.3 (Karplus and Diederichs, 2012). X-ray data were indexed, integrated, and scaled with HKL2000 (Otwinowski and Minor, 1997) (‘Monomer’) or XDS (Kabsch, 2010) (W196A). X-ray diffraction data statistics are shown in **Table S1**.

Both AIF mutant structures were solved by molecular replacement using either monomeric wild-type AIF (PDB: 4BV6 for Monomer) or dimeric wild-type AIF-CTC (PDB: 4BUR for W196A; NAD ligands removed) as search models in Phaser (Mccoy et al., 2007). Models were built and corrected using COOT (Emsley et al., 2010) with refinement in Phenix (Adams et al., 2010). FAD, glycerol, and HEPES ligand restraints were created through the Phenix module eLBOW (Moriarty et al., 2009) using geometry optimization in eLBOW (glycerol, HEPES) or Mogul (FAD) (Bruno et al., 2004) and included as external files in the refinement. Side chain atoms lacking observable density were excluded or set to zero occupancy during refinement (Monomer: D183, K194, Q215, K388, K571, K388, K571, K583, L617; W196A: chain A – K189, K199, E346, K510, K571, E599; chain B – K127, K194, K199, K301, R324, K337, R358, Q370, K382, K384, K388, E405, K408, K510, K571, E599). The AIF78 Monomer structure was refined to an R_{factor} = 15.7% and an R_{free} = 19.4%, and the AIF78 W196A structure was refined to an R_{factor} = 20.2% and an R_{free} = 24.0%. Crystallographic data statistics are shown in **Table S1**. 100% (AIF78 Monomer) and 99.8% (AIF78 W196A) of all residues are in favored and allowed regions of the Ramachandran plot. Backbone density for the two Ramachandran outliers of the W196A structure (R285, chains A and B) is well-defined. These residues participate in a network supporting the FAD cofactor, to which we attribute their non-standard torsion angle geometry. Other residues in this network, such as K177, also exhibit borderline, though not outlier, Ramachandran values. All structural figures were prepared using PyMOL (www.pymol.org). Angles between β-strands were calculated with open-source scripts (Thomas Holder, ‘anglesbetweenhelices.py’, 2010). AIF78 monomer and AIF78 W196A structures have been deposited with the PDB under accession codes 5KVI and 5KVH respectively.

All-Atom Molecular Dynamics Simulations and Analysis

Free AIF and AIF/FADH-/NAD+ Starting Structures

The starting structure for simulating ligand-free AIF was prepared from published coordinates of human wild-type AIF (PDB: 4BV6), and missing residues from the disordered C-loop (residues 546-558) were added using SYBYL-X 2.1.1 (Certara). This model was subsequently used to generate the starting structure for AIF-CTC, where the FAD cofactor was modeled in its reduced form ($\mathrm{FADH^-}$) by addition of a hydrogen to N5 of the isoalloxazine ring with SYBYL-X 2.1.1 setting the cofactor to a final charge of

-2. Coordinates for the NAD^+ ligand from the AIF-CTC crystal structure (PDB: 4BUR) were superimposed into the active site, and the active site was subsequently allowed to 'relax' around the ligand to assume the ligand-bound state during the simulation period. AMBER force field compliant parameters and topologies for the cofactors were generated with Antechamber (Wang et al., 2006).

To distinguish structural changes originating from crystallographic relaxation in the force field from those arising from CTC formation, a second AIF-CTC starting structure was prepared using coordinates extracted from the equilibrated portion of the ligand-free AIF trajectory and a similar superposition of the parameterized $FADH^-$ cofactor and NAD^+ ligand. Residues within 6 Å of the active site of the relaxed structure were manually adjusted to allow accommodation of the NAD^+ ligand and the simulation was run following the same procedure as below. Subsequent analysis revealed similar outcomes from both AIF-CTC trajectories.

Molecular Dynamics Simulations

Simulations were run with GROMACS 4.6.7. (Pronk et al., 2013; Van der Spoel et al., 2005) at 300 K using the AMBER ff03 force field (Duan et al., 2003) with the TIP3P explicit solvent model (Jorgensen et al., 1983). Starting structures were equilibrated by placing them in a dodecahedral water box extending one nm beyond the protein in all dimensions, and sodium counterions were added to achieve electrostatic neutrality. Each system was energy minimized with the steepest descent algorithm until the maximum force fell below 1000 kJ/mol/min, using a step size of 0.01 nm and a cutoff distance of 1.2 nm for the neighbor list, Coulomb interactions, and van der Waals interactions. The system was equilibrated for 1.0 nanoseconds under periodic boundary conditions using the particle-mesh Ewald method for the long-range evaluation of electrostatic forces (Essmann et al., 1995). For production runs, all bonds were constrained with the LINCS algorithm (Hess, 2008) and virtual sites (Feenstra et al., 1999) were used to allow a 4 fs time step. Cut-offs of 1.0 nm were used for the neighbor list, Coulomb interactions, and van der Waals interactions. The Verlet cutoff scheme was used for the neighbor list. The stochastic velocity rescaling (v-rescale) thermostat (Bussi et al., 2007) was used to hold the temperature at 300 K. Production runs extended for 500 ns with a step size of 3 fs.

Analysis of AIF Trajectories

To account for model relaxation from the crystallographic into the forcefield environment, backbone RMSD plots of C-loop residues 509-559 relative to the starting structure were assessed visually over the course of the trajectory. The RMSD reached an equilibrium point relative to the starting structure within the first 15-60 ns of each trajectory, and the simulation period beyond this point was used for further analysis
(AIF #1 and #2 -- 60-500 ns; AIF-CTC crystal starting structure -- 25-500 ns; AIF-CTC relaxed starting structure -- 15-500 ns).

RMSD calculations were generated with the RMSDTT plugin (Luis Gracia, https://github.com/luisico/rmsdtt) of the VMD molecular visualization program (Humphrey et al., 1996). Electrostatic interactions between residues were quantified based on occupancy using the HBonds plugin (JC Gumbart and Dong Luo http://www.ks.uiuc.edu/Research/vmd/plugins/hbonds/) and Salt Bridges (Leonardo Trabuco and Elizabeth Villa http://www.ks.uiuc.edu/Research/vmd/plugins/saltbr/) analysis modules within VMD.

Dihedral Mutual Information Analysis

Communication between active site residues K177, F310, E314, E453, H454, and S484 and the rest of AIF was quantified using Mutual Information (MI) between backbone and side chain dihedral angles similar to previous methods (Bowman and Geissler, 2012; McClendon et al., 2009). MI measures the dependence between two variables, X and Y, by quantifying probability of knowing the state of X given the state of Y. It is defined as:

$$I(X,Y) = \sum_{x\in X} \sum_{y\in Y} p(x,y) \log\left(\frac{p(x,y)}{p(x)p(y)}\right) \quad [1]$$

where p(x,y) represents the joint probability distribution between two dihedral angles X and Y, and p(x) represents the marginal probability distribution of dihedral X. For each simulation, ϕ, ψ, and χ angles for each residue were extracted using the MDTraj library (Version 1.5.1) (McGibbon et al., 2015) and assigned to *cis* or *trans* states (ϕ, ψ) or *gauche*+, *gauche*-, and *trans* rotameric states (χ). Dihedral MI values were subsequently computed for all residue pairs with Equation 1 conducted with the CARDS framework using in-house scripts to generate a symmetric MI matrix (Singh and Bowman, manuscript in preparation).

Communication between a specific AIF residue and the collective active site set (K177, F310, E314, E453, H454, S484) was computed from paired dihedral MI values as follows. First, an adjusted MI for each residue-active site residue pair was calculated by summing the dihedral MI value for the residue of interest with the dihedral MI values for all neighboring residues (within 6 Å of its sidechain). This was done to capture indirect communication between a given residue and an active site residue that is mediated through contacts with its neighboring residues. This adjusted MI was then summed across all six residue-active site residue pairs to produce the total MI from a given residue to the active site as a whole.

To ensure that the aggregate simulation time was sufficient to provide a robust estimate of MI-based communication, Pearson correlation coefficients between total MI values were calculated between replicate 500-ns simulations for the ligand-free (0.86) and the CTC (0.81) trajectories, indicating that the system was sampled adequately to estimate MI. Color structure maps of MI were prepared in PyMOL (www.pymol.org).

Supplemental References

Adams, P.D., Afonine, P.V., Bunkoczi, G., Chen, V.B., Davis, I.W., Echols, N., Headd, J.J., Hung, L.W., Kapral, G.J., Grosse-Kunstleve, R.W.*, et al.* (2010). PHENIX: a comprehensive Python-based system for macromolecular structure solution. Acta Crystallographica Section D-Biological Crystallography *66*, 213-221.

Bowman, G.R., and Geissler, P.L. (2012). Equilibrium fluctuations of a single folded protein reveal a multitude of potential cryptic allosteric sites. Proceedings of the National Academy of Sciences of the United States of America *109*, 11681-11686.

Bruno, I.J., Cole, J.C., Kessler, M., Luo, J., Motherwell, W.D., Purkis, L.H., Smith, B.R., Taylor, R., Cooper, R.I., Harris, S.E.*, et al.* (2004). Retrieval of crystallographically-derived molecular geometry information. J Chem Inf Comput Sci *44*, 2133-2144.

Bussi, G., Donadio, D., and Parrinello, M. (2007). Canonical sampling through velocity rescaling. Journal of Chemical Physics *126*, 014101.

Classen, S., Hura, G.L., Holton, J.M., Rambo, R.P., Rodic, I., McGuire, P.J., Dyer, K., Hammel, M., Meigs, G., Frankel, K.A.*, et al.* (2013). Implementation and performance of SIBYLS: a dual endstation small-angle X-ray scattering and macromolecular crystallography beamline at the Advanced Light Source. Journal of Applied Crystallography *46*, 1-13.

Cormier, C.Y., Mohr, S.E., Zuo, D., Hu, Y., Rolfs, A., Kramer, J., Taycher, E., Kelley, F., Fiacco, M., Turnbull, G.*, et al.* (2010). Protein Structure Initiative Material Repository: an open shared public resource of structural genomics plasmids for the biological community. Nucleic Acids Res *38*, D743-749.

Duan, Y., Wu, C., Chowdhury, S., Lee, M.C., Xiong, G.M., Zhang, W., Yang, R., Cieplak, P., Luo, R., Lee, T.*, et al.* (2003). A point-charge force field for molecular mechanics simulations of proteins based on condensed-phase quantum mechanical calculations. Journal of Computational Chemistry *24*, 1999-2012.

Dyer, K.N., Hammel, M., Rambo, R.P., Tsutakawa, S.E., Rodic, I., Classen, S., Tainer, J.A., and Hura, G.L. (2014). High-throughput SAXS for the characterization of biomolecules in solution: a practical approach. Methods Mol Biol *1091*, 245-258.

Emsley, P., Lohkamp, B., Scott, W.G., and Cowtan, K. (2010). Features and development of Coot. Acta Crystallographica Section D-Biological Crystallography *66*, 486-501.

Essmann, U., Perera, L., Berkowitz, M.L., Darden, T., Lee, H., and Pedersen, L.G. (1995). A Smooth Particle Mesh Ewald Method. Journal of Chemical Physics *103*, 8577-8593.

Feenstra, K.A., Hess, B., and Berendsen, H.J.C. (1999). Improving efficiency of large time-scale molecular dynamics simulations of hydrogen-rich systems. Journal of Computational Chemistry *20*, 786-798.

Franke, D., and Svergun, D.I. (2009). DAMMIF, a program for rapid ab-initio shape determination in small-angle scattering. Journal of Applied Crystallography *42*, 342-346.

Hess, B. (2008). P-LINCS: A parallel linear constraint solver for molecular simulation. Journal of Chemical Theory and Computation *4*, 116-122.

Humphrey, W., Dalke, A., and Schulten, K. (1996). VMD: Visual molecular dynamics. Journal of Molecular Graphics & Modelling *14*, 33-38.

Hura, G.L., Budworth, H., Dyer, K.N., Rambo, R.P., Hammel, M., McMurray, C.T., and Tainer, J.A. (2013). Comprehensive macromolecular conformations mapped by quantitative SAXS analyses. Nat Methods *10*, 453-454.

Jorgensen, W.L., Chandrasekhar, J., Madura, J.D., Impey, R.W., and Klein, M.L. (1983). Comparison of Simple Potential Functions for Simulating Liquid Water. Journal of Chemical Physics *79*, 926-935.

Kabsch, W. (2010). Xds. Acta Crystallographica Section D-Biological Crystallography *66*, 125-132.

Karplus, P.A., and Diederichs, K. (2012). Linking crystallographic model and data quality. Science *336*, 1030-1033.

McClendon, C.L., Friedland, G., Mobley, D.L., Amirkhani, H., and Jacobson, M.P. (2009). Quantifying Correlations Between Allosteric Sites in Thermodynamic Ensembles. Journal of Chemical Theory and Computation *5*, 2486-2502.

Mccoy, A.J., Grosse-Kunstleve, R.W., Adams, P.D., Winn, M.D., Storoni, L.C., and Read, R.J. (2007). Phaser crystallographic software. Journal of Applied Crystallography *40*, 658-674.

McGibbon, R.T., Beauchamp, K.A., Harrigan, M.P., Klein, C., Swails, J.M., Hernandez, C.X., Schwantes, C.R., Wang, L.P., Lane, T.J., and Pande, V.S. (2015). MDTraj: A Modern Open Library for the Analysis of Molecular Dynamics Trajectories. Biophysical Journal *109*, 1528-1532.

Moriarty, N.W., Grosse-Kunstleve, R.W., and Adams, P.D. (2009). electronic Ligand Builder and Optimization Workbench (eLBOW): a tool for ligand coordinate and restraint generation. Acta Crystallographica Section D-Biological Crystallography *65*, 1074-1080.

Otwinowski, Z., and Minor, W. (1997). Processing of X-ray diffraction data collected in oscillation mode. Macromolecular Crystallography, Pt A *276*, 307-326.

Pelikan, M., Hura, G.L., and Hammel, M. (2009). Structure and flexibility within proteins as identified through small angle X-ray scattering. General Physiology and Biophysics *28*, 174-189.

Petoukhov, M.V., Franke, D., Shkumatov, A.V., Tria, G., Kikhney, A.G., Gajda, M., Gorba, C., Mertens, H.D.T., Konarev, P.V., and Svergun, D.I. (2012). New developments in the ATSAS program package for small-angle scattering data analysis. Journal of Applied Crystallography *45*, 342-350.

Pettersen, E.F., Goddard, T.D., Huang, C.C., Couch, G.S., Greenblatt, D.M., Meng, E.C., and Ferrin, T.E. (2004). UCSF Chimera--a visualization system for exploratory research and analysis. Journal of Computational Chemistry *25*, 1605-1612.

Pronk, S., Pall, S., Schulz, R., Larsson, P., Bjelkmar, P., Apostolov, R., Shirts, M.R., Smith, J.C., Kasson, P.M., van der Spoel, D.*, et al.* (2013). GROMACS 4.5: a high-throughput and highly parallel open source molecular simulation toolkit. Bioinformatics *29*, 845-854.

Rambo, R.P., and Tainer, J.A. (2013). Accurate assessment of mass, models and resolution by small-angle scattering. Nature *496*, 477-481.

Schneidman-Duhovny, D., Hammel, M., Tainer, J.A., and Sali, A. (2013). Accurate SAXS profile computation and its assessment by contrast variation experiments. Biophysical Journal *105*, 962-974.

Seiler, C.Y., Park, J.G., Sharma, A., Hunter, P., Surapaneni, P., Sedillo, C., Field, J., Algar, R., Price, A., Steel, J.*, et al.* (2014). DNASU plasmid and PSI:Biology-Materials repositories: resources to accelerate biological research. Nucleic Acids Res *42*, D1253-1260.

Van der Spoel, D., Lindahl, E., Hess, B., Groenhof, G., Mark, A.E., and Berendsen, H.J.C. (2005). GROMACS: Fast, flexible, and free. Journal of Computational Chemistry *26*, 1701-1718.

Volkov, V.V., and Svergun, D.I. (2003). Uniqueness of ab initio shape determination in small-angle scattering. Journal of Applied Crystallography *36*, 860-864.

Wang, J.M., Wang, W., Kollman, P.A., and Case, D.A. (2006). Automatic atom type and bond type perception in molecular mechanical calculations. Journal of Molecular Graphics & Modelling *25*, 247-260.

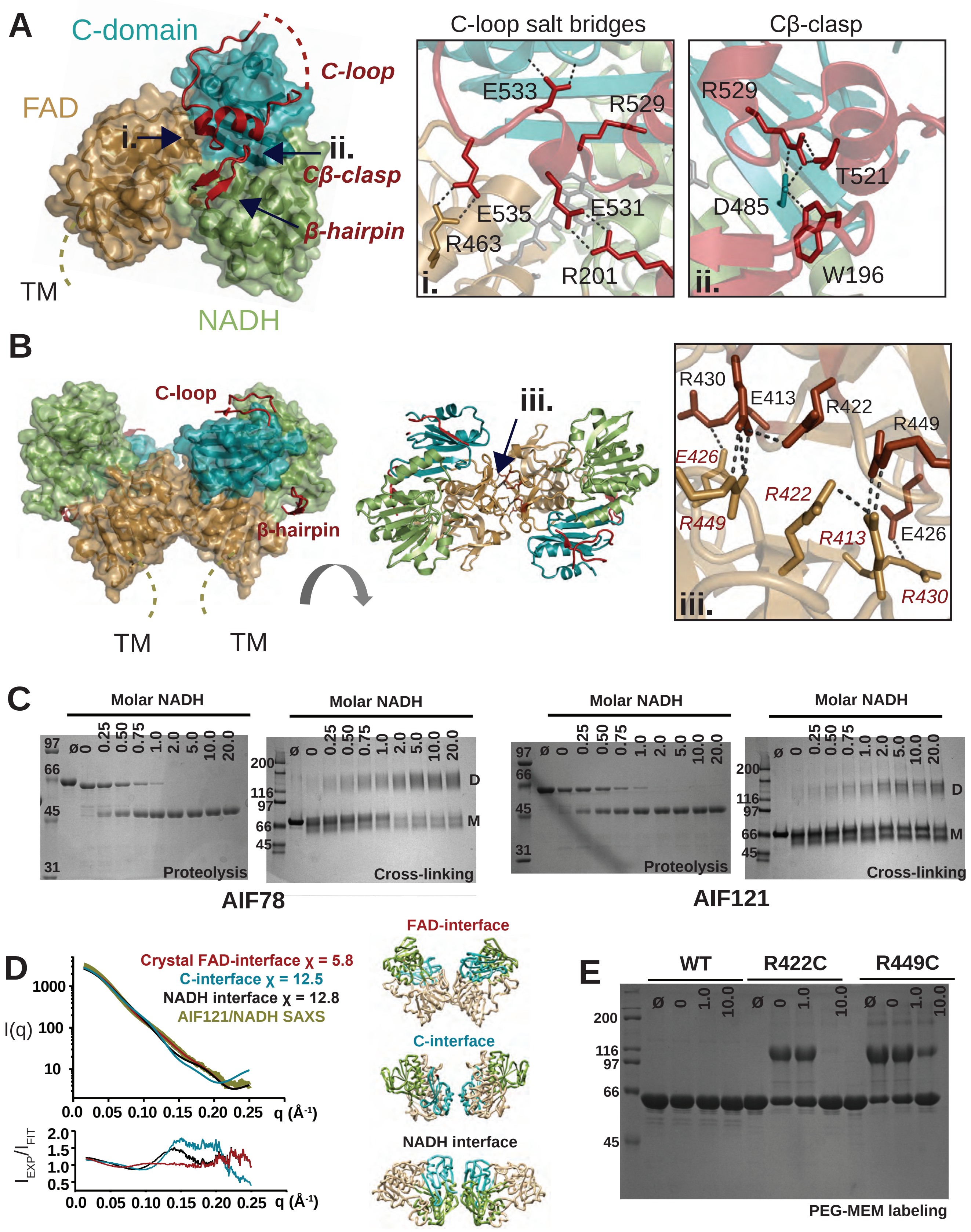

Figure S1 to accompany Figure 1. (A) Monomeric AIF domain and motif organization (*left*) with TM indicating transmembrane tether. Enlarged views of C-loop residues forming salt bridges with the protein core (*i, middle*) or participating in the Cβ-clasp (*ii, right*). PDB: 4BV6 **(B)** Dimeric AIF (*left*) and residues participating in the dimerization interface (iii, *right*). PDB: 4BUR. **(C)** Proteinase K limited proteolysis of AIF78 (*left*) and AIF121 (*right*) demonstrates exposure of the C-loop to solvent, while BS^3 cross-linking confirms dimerization in the presence of molar excess NADH (M = monomer, D = dimer). **(D)** Theoretical SAXS profiles and fit ratios (*left)* for alternate AIF dimers (*right*) overlayed with AIF121/NADH SAXS data. **(E)** PEG-MEM labeling of AIF78 wild-type, R422C, and R449C at 0-, 1- or 10-fold molar excess NADH.

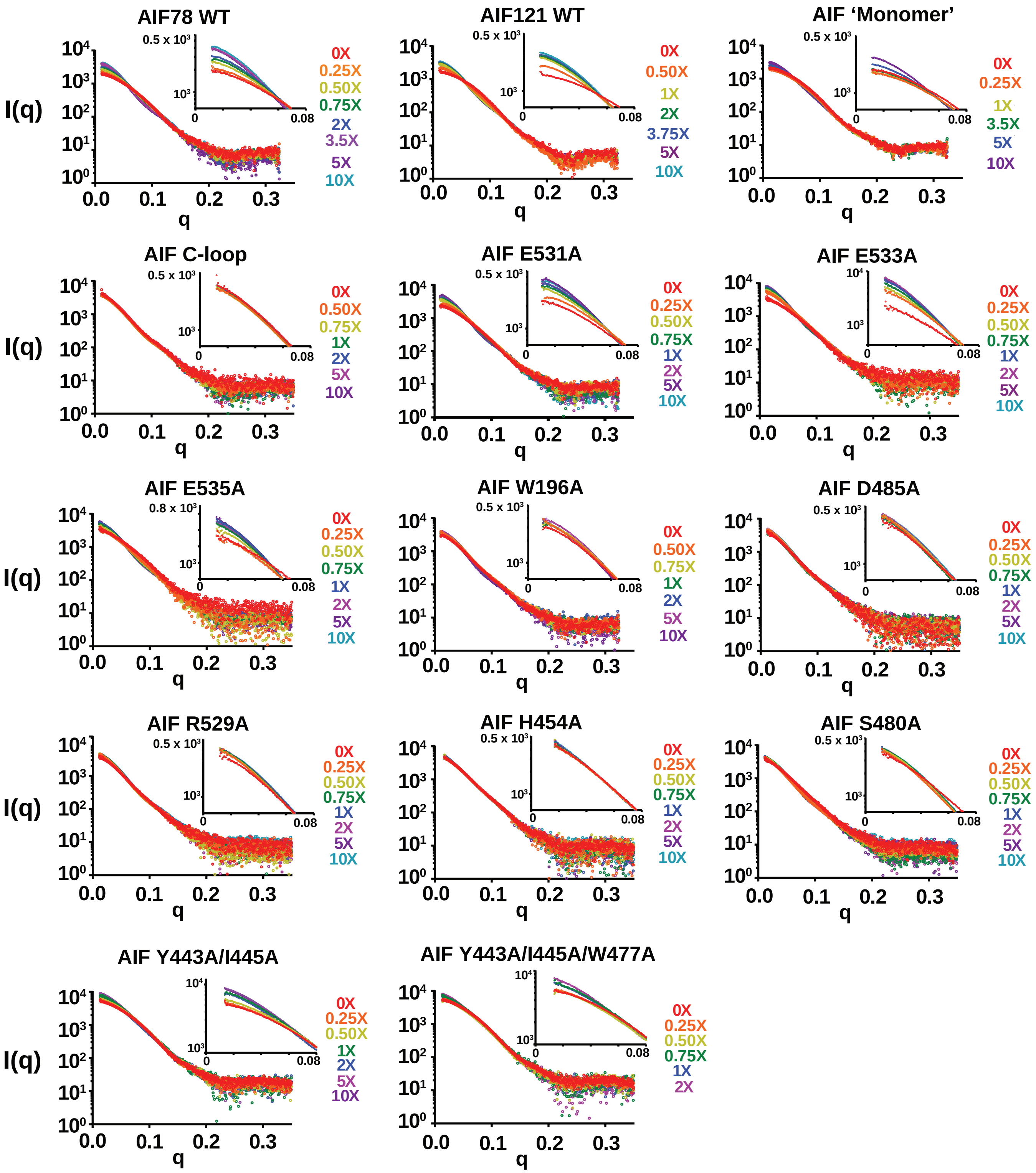

Figure S2 to accompany Figures 1, 2, and 5. SAXS I(q) curves from wild-type and mutant AIF NADH titrations. Insets show expanded low-Q region. AIF 'Monomer' 0X has been scaled to match the concentration of the remaining curves of the series.

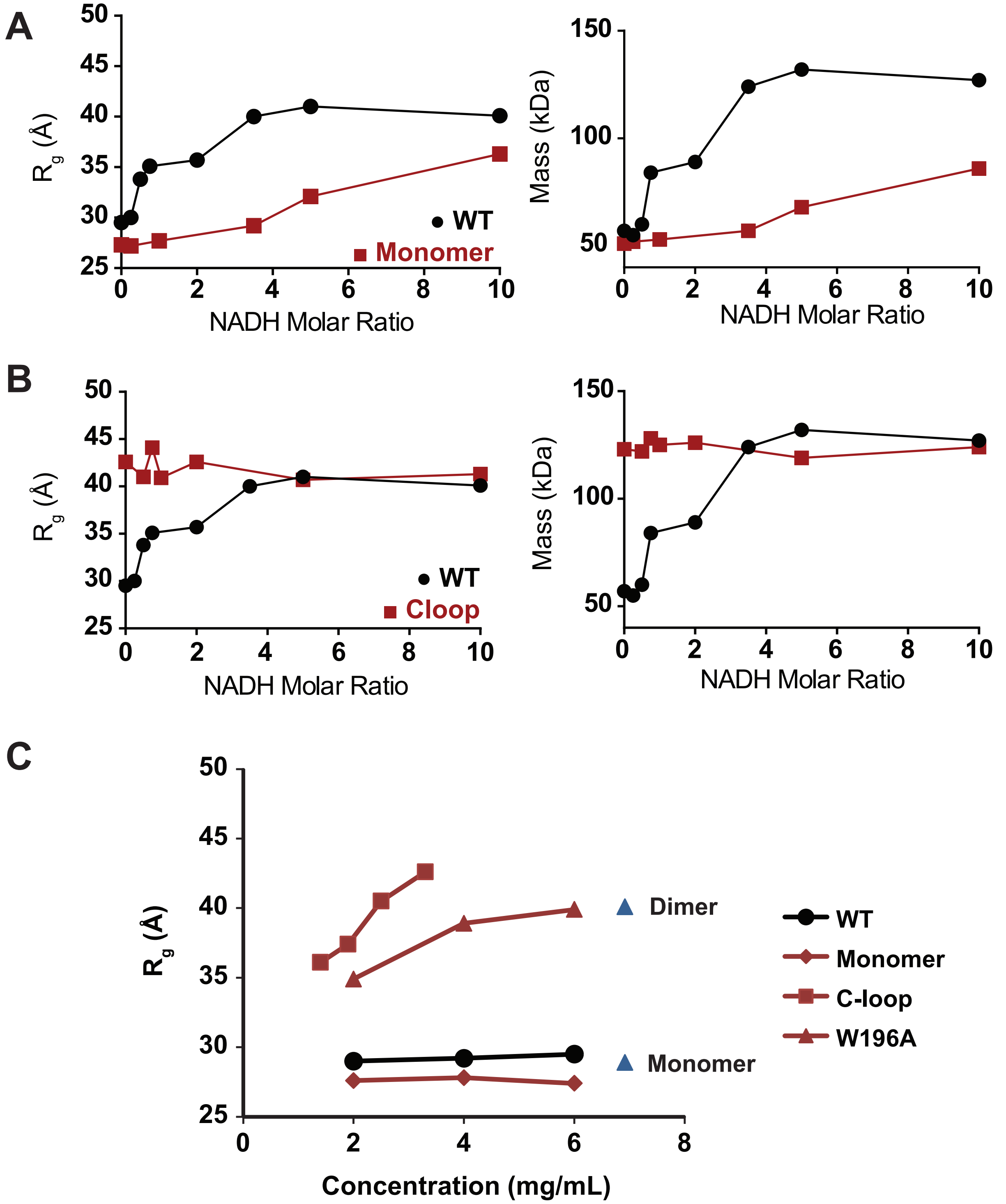

Figure S3 to accompany Figure 2. (A) SAXS R_g and mass analyses of AIF78 monomer (E413A/E422A/E430A) show a rise in R_g, but not mass, with increasing NADH concentration. **(B)** SAXS R_g and mass analyses for AIF78 C-loop show the mutant to be dimeric in the absence of ligand across all NADH concentrations. **(C)** R_g analysis of wild-type and mutant AIF shows stable R_g values for wild-type AIF and monomeric mutants and a concentration-dependent rise to dimeric Rg values for dimer-permissive mutants. Blue triangles reference R_g values for AIF78 with or without 10-fold molar excess NADH at 4 mg/mL.

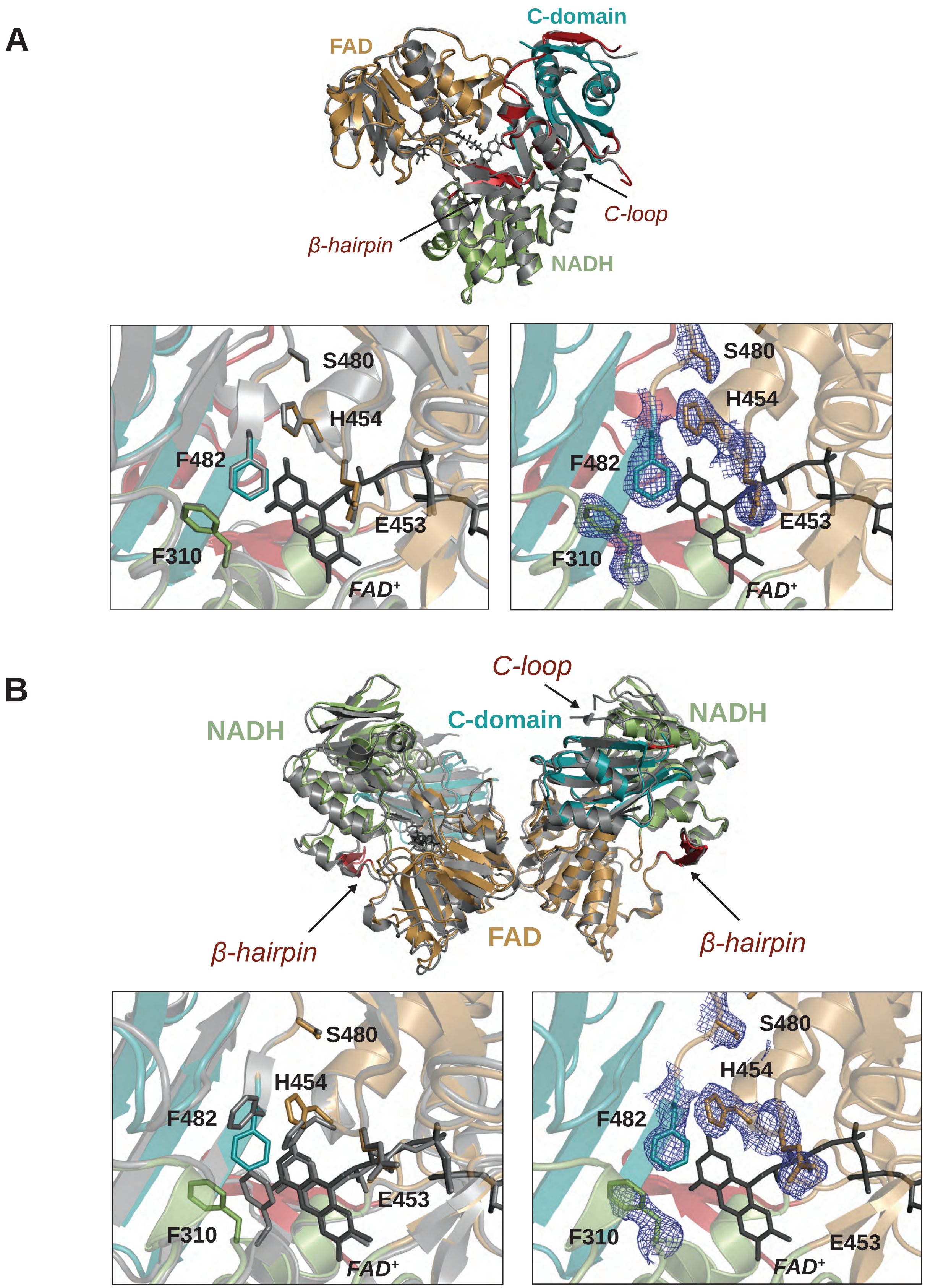

Figure S4 to accompany Figure 3. Overlay of AIF78 Monomer (E413A/R422A/R430A) **(A)** and W196A **(B)** crystal structures (color) with wild-type AIF coordinates (gray) (PDB:4BV6 (A) or 4BUR (B)). β-hairpin and C-loop residues are shown in red. Lower panels display close-ups of the active site with wild-type structures (*left*) or simulated annealing |Fo-Fc| omit electron density maps contoured at 2.5σ and carved at 1.8 Å radius (*right*).

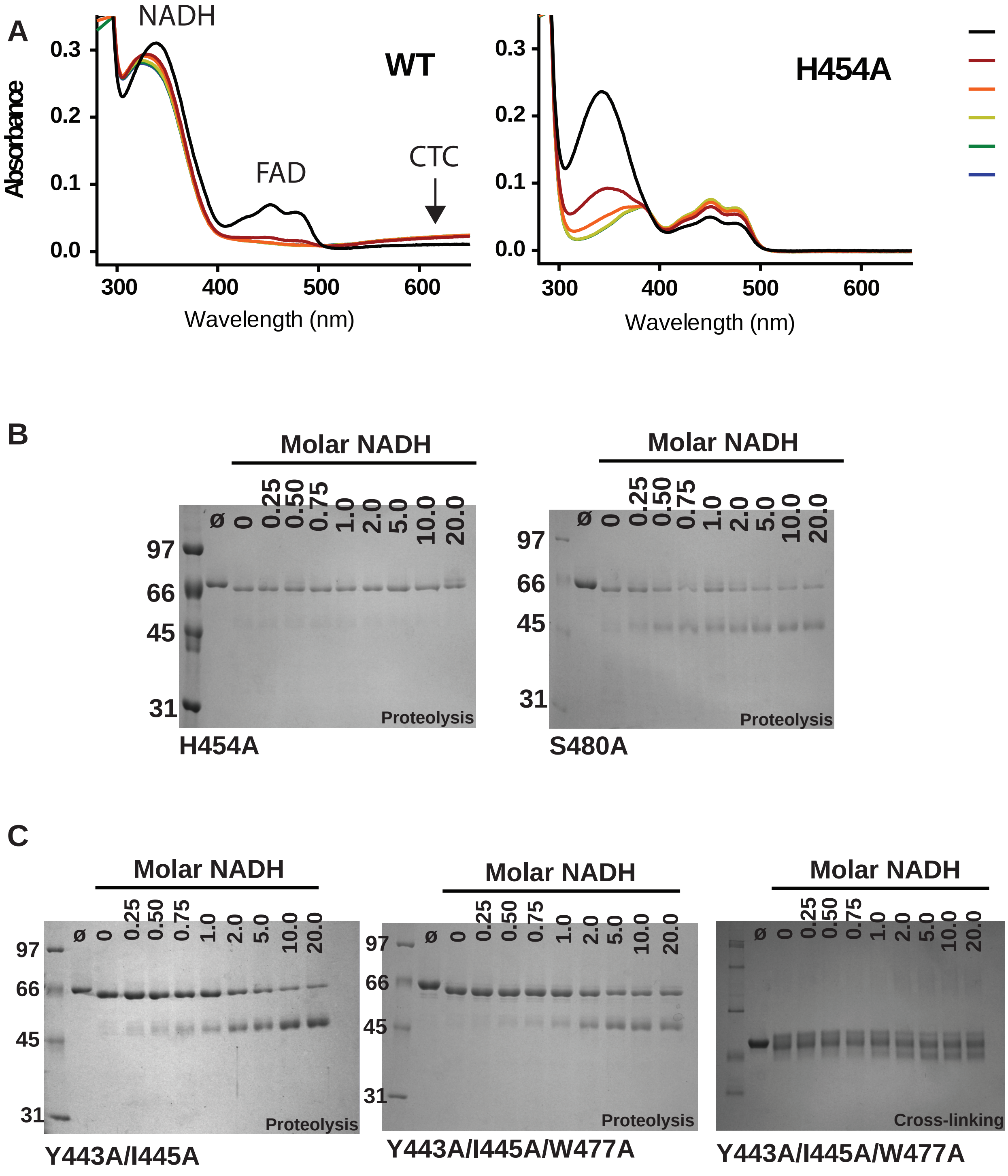

Figure S5 to accompany Figure 5. (A) UV-Vis absorbance scans of wild-type (*top*) or H454A (*bottom*) AIF78 in the presence of 5-fold molar excess NADH at the indicated times after mixing. The absorption rise at >600 nm signaling CTC formation is absent in H454A and the 340 nm absorption peak from reduced NADH decreases over time as NADH is oxidized to NAD$^+$ by the mutant. **(B)** Limited proteolysis analysis AIF78 H454A and S480A. **(C)** Limited proteolysis analysis of double and triple mutants of the hydrophobic border (*left, middle*) and BS^3 cross-linking analysis of the triple mutant (*right*).

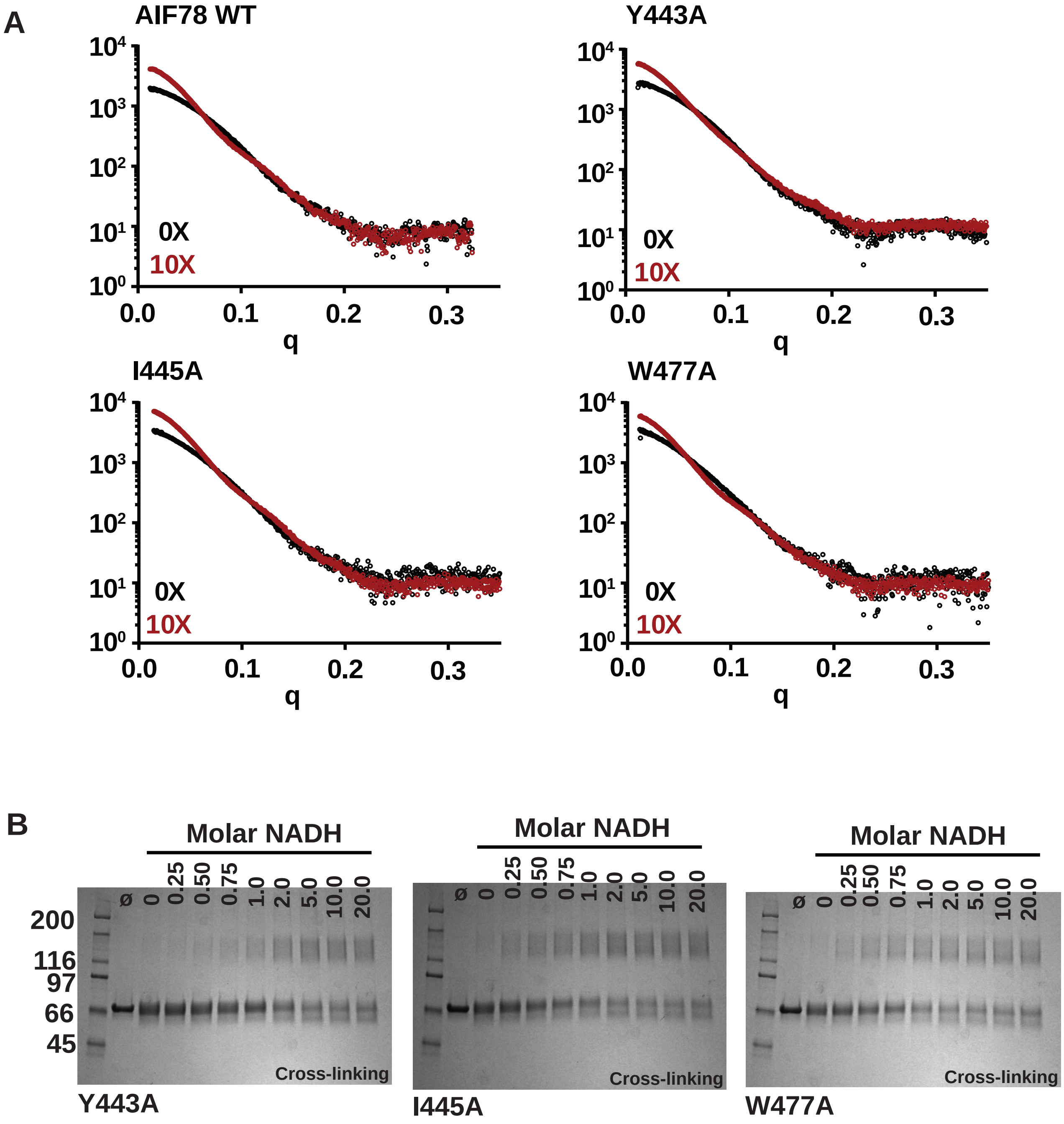

Figure S6 to accompany Figure 5. (A) SAXS I(q) profiles for wild-type and mutant AIF in the absence and presence of excess NADH demonstrate intact dimerization of single mutants of the hydrophobic border. (B) Cross-linking analyses of hydrophobic border mutants with increasing molar NADH also exhibit intact dimerization.

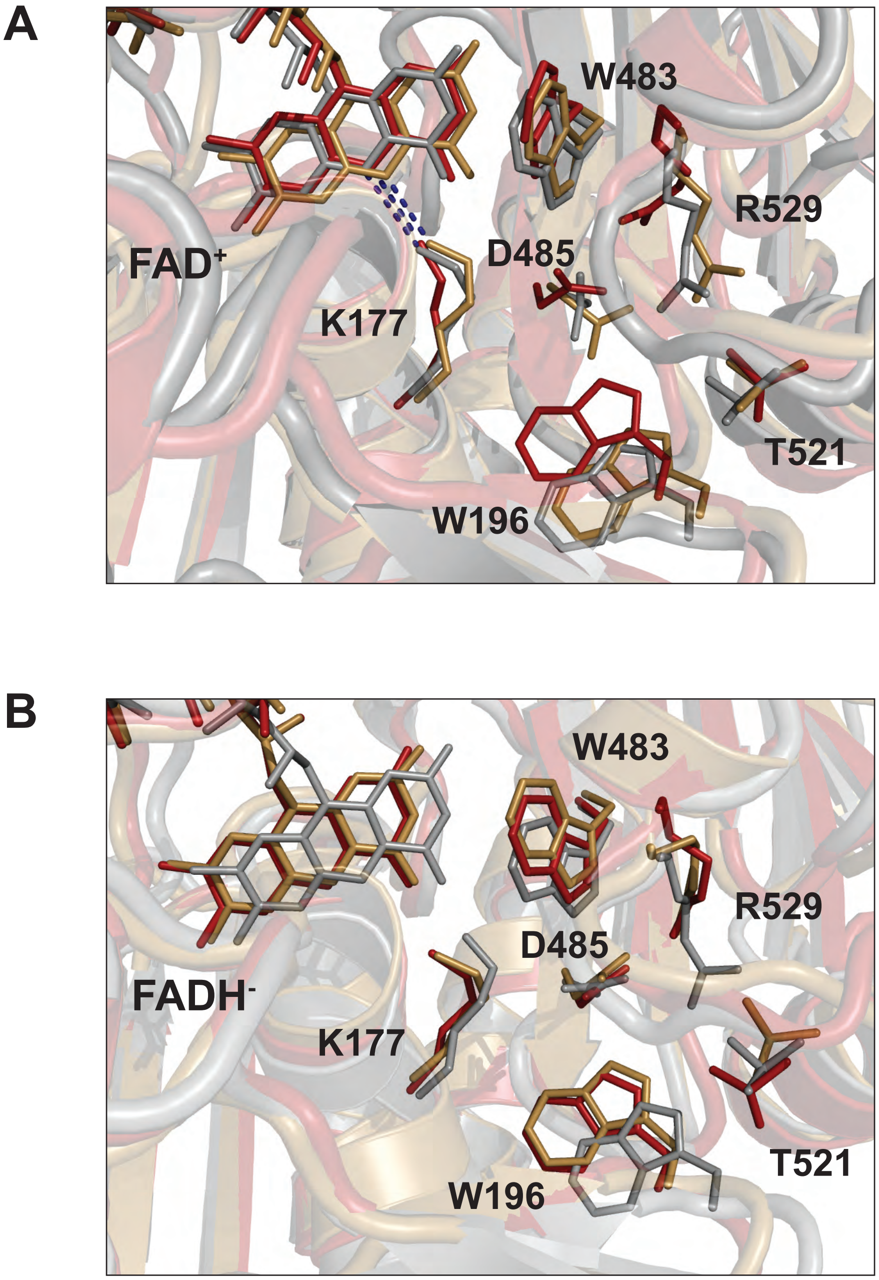

Figure S7 to accompany Figure 7. Overlay of selected frames from ligand-free **(A)** and CTC **(B)** simulations of AIF highlighting the FAD cofactor and Cβ-clasp. For ligand-free AIF, 60 ns (gray), 225 ns (gold), 500 ns (red). For AIF-CTC, 25 ns (gray), 225 ns (gold), 500 ns (red).

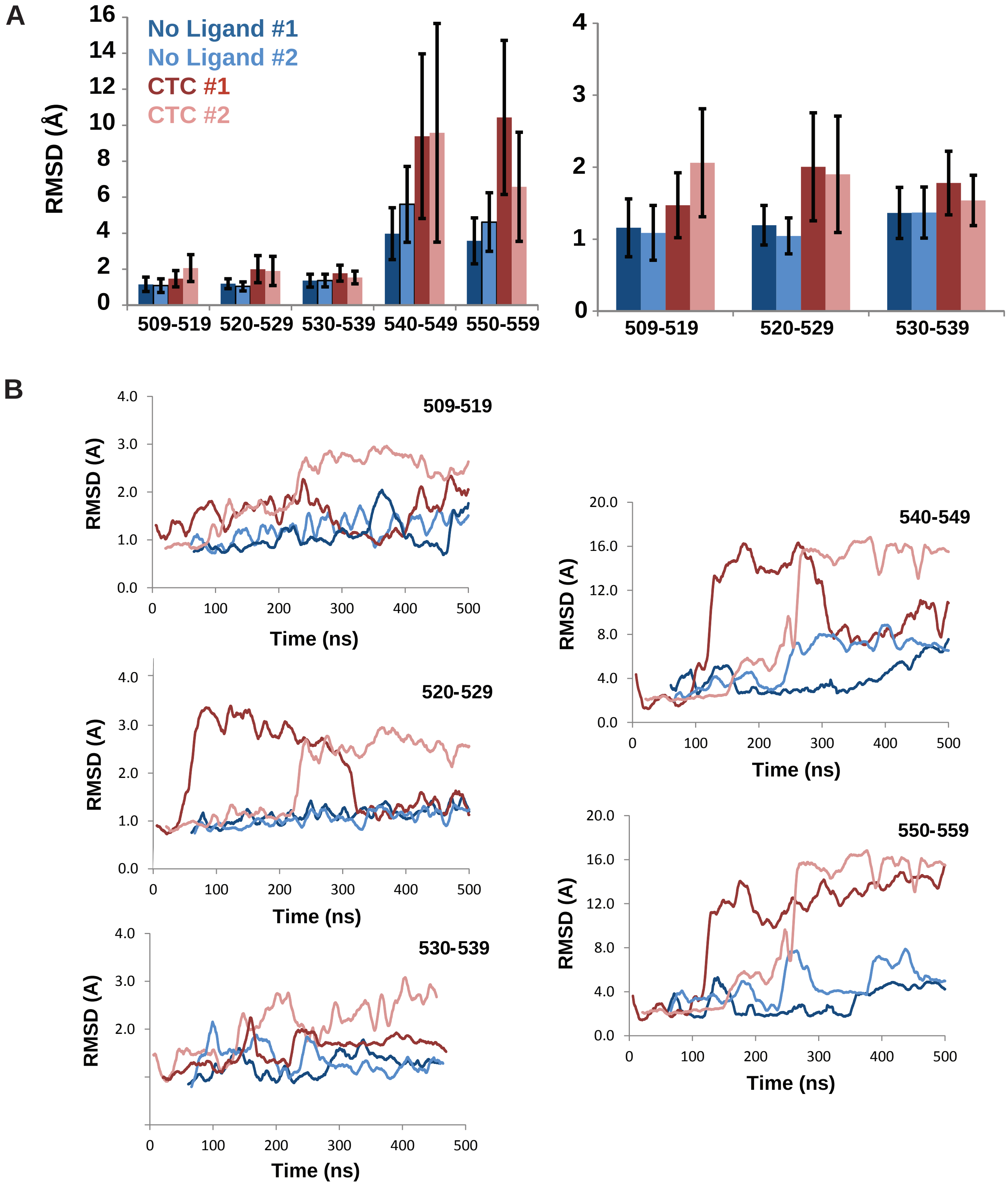

Figure S8 to accompany Figure 7. (A) Average RMSD values for 10-residue segments the C-loop for each trajectory. Error bars show standard deviation. **(B)** Smoothed RMSD values (10 ns window) plotted across the trajectory time course.